

RESEARCH ARTICLE

10.1002/2015JB012586

Key Points:

- Development of a regional gravity field modeling approach
- Optimal combination of heterogeneous data sets
- Additional value to existing global models

Correspondence to:

V. Lieb,
verena.lieb@tum.de

Citation:

Lieb, V., M. Schmidt, D. Dettmering, and K. Börger (2016), Combination of various observation techniques for regional modeling of the gravity field, *J. Geophys. Res. Solid Earth*, 121, doi:10.1002/2015JB012586.

Received 15 OCT 2015

Accepted 15 APR 2016

Accepted article online 27 APR 2016

Combination of various observation techniques for regional modeling of the gravity field

Verena Lieb¹, Michael Schmidt¹, Denise Dettmering¹, and Klaus Börger^{2,3}
¹Deutsches Geodätisches Forschungsinstitut der Technischen Universität München, Munich, Germany, ²Professur für Astronomische, Physikalische und Mathematische Geodäsie, Institut für Geodäsie und Geoinformation, Bonn, Germany, ³German Space Situational Awareness Centre, Uedem, Germany

Abstract Modeling a very broad spectrum of the Earth's gravity field needs observations from various measurement techniques with different spectral sensitivities. Typically, high-resolution regional gravity data are combined with low-resolution global observations. To exploit the gravitational information as optimally as possible, we set up a regional modeling approach using radial spherical basis functions, emphasizing the strengths of various data sets by the flexible combination of high- and middle-resolution terrestrial, airborne, shipborne, and altimetry measurements. The basis functions are defined and located in the region of interest in such a manner, which the highest measure of information of the input data is captured. Any functional of the Earth's gravity field can be derived, as, e.g., quasi-geoid heights or gravity anomalies. Here we present results of a study area in Northern Germany. A comprehensive cross validation to external observation data delivers standard deviations less than 5 cm. Differences to an existing regional quasi-geoid model count on average ± 6 cm and prove the plausibility of our solution. The comparison with existing global models reaches higher standard deviations for the more sensitive gravity anomalies as for quasi-geoid heights, showing the additional value of our solution in the high frequency domain. Covering a broad frequency spectrum, our regional models can be used as basis for various applications, such as refinement of global models, national geoid determination, and detection of mass anomalies in the Earth's interior.

1. Introduction

High-resolution gravity data sets are available only in some parts of the Earth. Typically, they stem from terrestrial, shipborne or airborne observations and reach a spatial resolution down to a few kilometers. Our aim is to extract the maximum gravitational information from a combination of all data and to model high-resolution regional gravity fields in those well-observed areas. The spectral content of the final models shall be expanded by combining them further with middle- and low-resolution satellite measurements, especially from altimetry. In contrast to global gravity field modeling, we adapt a regional approach by being both spatially and spectrally as close as possible to the observations without suffering the loss of accuracy due to data gaps.

During the last decades, various methods of regional gravity modeling have been proposed and further developed by combining different observation types. The statistical method of least squares collocation (LSC), for instance, has been developed in the 1970s and 1980s [Krarup, 1970; Moritz, 1978; Koch, 1977]. One of the key advantages of LSC is that it provides together with regional gravity field and geoid models from different gravity data types, error information in the form of variances, or even full variance-covariance matrices. Reguzzoni and Sansò [2012] discuss in detail a possible method for the combination of high-resolution and satellite-only gravity field models.

An alternative approach is based on spherical radial basis functions (SBF) [e.g., Freeden et al., 1998; Schmidt et al., 2007]. They are isotropic and characterized by their localizing feature. For this reason they are an appropriate tool to consider the heterogeneity of data sources (satellite, airborne, terrestrial, etc.), frequency content, sampling geometry, and observation stochastic. SBFs are usually defined on a regular point grid on a sphere and can be easily adapted to the frequency content of the signal under investigation. Following this concept, a priori variances of the modeled signal can be used to construct the so-called spherical splines [Eicker et al., 2013]. Another approach uses Poisson multipole wavelets which allow a physical interpretation as masses in the Earth's interior; the localization properties of these wavelets can be used to combine

heterogeneous data [e.g., *Panet et al.*, 2006]. *Bentel et al.* [2013a] studied various different spherical basis functions for their application in regional gravity modeling. The relation of SBFs to spherical harmonics (SH), as well as the choice of several specific parameters, is justified by the findings of *Bentel et al.* [2013b] and *Naeimi* [2013].

Due to the different spectral content of complementary observations techniques, *Haagmans et al.* [2002] set up a multiresolution representation (MRR) for regional geoid determination by combining a low-pass-filtered global geopotential model with band-pass-filtered satellite gradiometer and regional high-pass-filtered gravity data. *Schmidt et al.* [2007], e.g., applied a MRR based on the mathematical formulation as suggested by *Freeden et al.* [1998].

To cover a wide range of the gravity field signal spectrum, regional models can be placed on the top of a highly accurate global gravity model, usually based on SH basis functions. We distinguish satellite-only combination models including GRACE (Gravity Recovery and Climate Experiment) [Tapley et al., 2004], GOCE (Gravity field and steady-state Ocean Circulation Explorer) [Rummel et al., 2002], and other satellite-related data sources, such as the GOCO (Gravity Observation Combination) series [Pail et al., 2010] and combination models including terrestrial and altimetric gravity field data, such as EGM2008 (Earth Gravitational Model 2008) [Pavlis et al., 2012]. The latter further enhances the spatial resolution apparently on a global scale, but, in fact, only in regions where a reasonable terrestrial data basis is available.

In this paper we present a method of regional gravity field modeling from the combination of various observation techniques, which enables on the one hand to extract the maximum spectral content out of each measurement system and, on the other hand, to manage different observation heights, accuracies, and resolutions. We focus on a flexible approach for the combination of real data considering all their specific features. The methodology delivers the potential and prepares the ground for establishing a MRR in future research.

For the objectives of this manuscript, we first introduce the different data sets in a study area in *Northern Germany* and emphasize their peculiarities (cf. section 2). We then present the modeling procedure adapted to the variety of data using SBFs (cf. section 3); in the first part (cf. section 3.1) we describe the fundamentals, tools, and settings of our method, giving a kind of “recipe.” The discretization of the frequency spectrum in section 3.1.5 delivers the basis for combining the different data sets by their appropriate classification. In the second part (section 3.2), the estimation model is established at an appropriate resolution level. Formulating the observation equations and estimating the unknown coefficients are the key aspects. We combine the heterogeneous data sets on normal equation level, set up a full stochastic model, and are able to derive any functional of the Earth’s gravity field including full error propagation. In section 4 we finally apply the approach to the data of section 2; we discuss the relative weighting of the data sets by variance component estimation (VCE) and comment upon the resulting gravitational structures in the study area exemplarily for gravity anomalies and quasi-geoid heights. Besides deriving the precision of the results from the stochastic part, we evaluate the results externally by cross validation in order to verify the model fit to the data and the reasonable parametrization of our approach. A comparison with the regional model GCG2011 (German Combined QuasiGeoid 2011) further verifies the plausibility of our solution, while a comparison with the global gravity model EGM2008 indicates the differences between global and regional approaches. We summarize the benefits and the additional value of our regional approach in section 5.

2. Study Area and Gravity Observations

Our study area is located in the north of Germany from 6.2° to 14.0° longitude and from 53.5° to 55.0° latitude (cf. Figure 1, green bordered). It thus contains both onshore and offshore areas which vary in their gravitational structure and therefore allows the combination of various of data sets. Figure 1 shows the spatial distribution of the different data sets, projected on the Earth’s surface. Over the sea, measurements from middle-resolution altimetry missions are available (dark green dots in Figure 1), supplemented by shipborne measurements (dark red dots) in the *Baltic Sea*. High-resolution airborne gravimetry observations cover ocean as well as land surface (orange lines). The largest data set consists of terrestrial observations (yellow dots) with a very high spectral and spatial resolution due to precise gravity measurement systems and the density of observation sites from 53.5° in the south up to the German coastlines in the north. As the single data sets are based on diverse measurement techniques with different spatial and spectral resolutions and accuracies, we apply a VCE (see section 4) as one among other possible instruments, to handle these inhomogeneities properly,

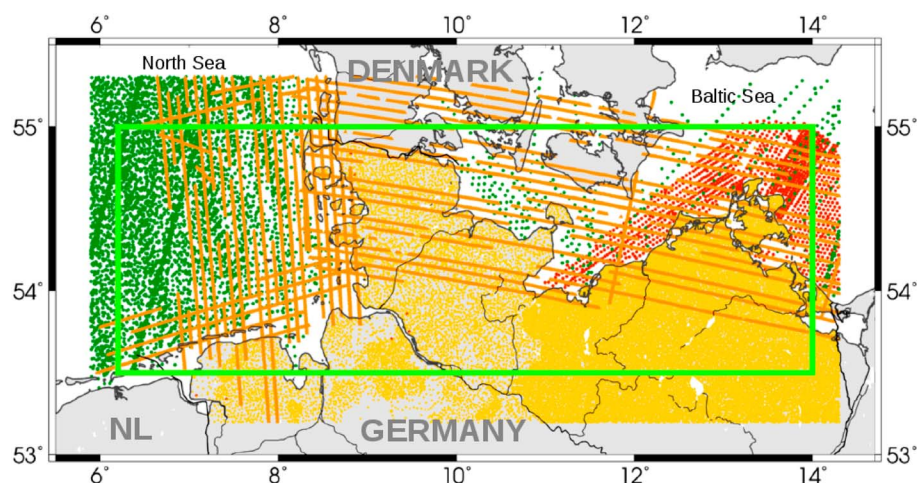


Figure 1. Distribution of the observations in the test area Northern Germany (green bordered). In dark green we display the observation sites from satellite altimetry data; in red, orange, and yellow are the ones from shipborne, airborne, and terrestrial data. Thin black lines mark rivers and canals.

and thus abandon here a qualitative comparison. Additional prior information is obtained from a global SH model containing satellite gravimetry information.

2.1. Terrestrial Data

The terrestrial gravity data sets are provided in terms of absolute gravity g by the surveying offices of different federal states in Germany: *Schleswig-Holstein*, *Mecklenburg-West Pomerania*, and *Lower Saxony* (see yellow observation sites in Figure 1). They are supplemented by gravity measurements (taken in the 1950s) from the German gravity archive and from DGFI/IfAG (Institut für angewandte Geodäsie, Frankfurt). The BKG (Bundesamt für Kartographie und Geodäsie, Frankfurt/Leipzig) made the data available to us. We reference the gravity measurements to the ellipsoid GRS80 (Geodetic Reference System 1980) [Moritz, 2000] and use in the following gravity disturbances δg . In Mecklenburg-West Pomerania and Schleswig-Holstein the spatial resolution of the data is very high (<1 km), whereas in Lower Saxony the spatial resolution is lower due to data gaps of several kilometers. However, we reach approximately an average point distance of 5 km for the whole terrestrial data set.

2.2. Airborne Measurements

The airborne data sets are obtained from two flight campaigns, one over the Baltic Sea in 2006 (east-west oriented flight tracks in Figure 1) and another one over the *North Sea* in 2007/2008 (north-south oriented flight tracks). They have been operated and preprocessed from the Danish National Space Center, Denmark in cooperation with BKG. During the Baltic Sea campaign, flight turbulences slightly reduced the accuracy of the observations, verified by a validation against terrestrial and shipborne measurements. The data are provided in terms of gravity disturbances δg ; the horizontal ellipsoidal coordinates are referred to ETRS89 (European Terrestrial Reference System 1989) [Boucher and Altamimi, 1992], reference ellipsoid GRS80; the heights are referenced to DHHN92 (Deutsches Haupthöhennetz 1992) [Weber, 1994], primary leveling network of Germany), and the gravity measurements to IGSN-71 (International Gravity Standardization Net 1971, [Morelli et al., 1971], official gravity datum worldwide). We use the data along their original flight tracks and reference the flight height to GRS80. The along- and cross-track resolution averages 10 km.

2.3. Shipborne Measurements

The red colored offshore data in the Baltic Sea (Figure 1) originate from shipborne measurements. The data set is derived from a prototype for gravimetric shipborne measurements after A. Graf [Neunhöfer et al., 1997] in the 1950s. It is provided, preprocessed, and projected at sea level height in terms of gravity anomalies Dg (referred to GRS80) by the federal state Mecklenburg-West Pomerania. As the data stem from the early period of shipborne gravimetry, we assume low accuracy. Detailed information is not available. The spatial resolution averages 4 km.

2.4. Altimetry Missions

Satellite altimetry measures sea surface heights (SSH) along the satellite's ground track by analyzing the travel time of a radar signal between the satellite-based altimeter instrument and the ocean surface. In order to

convert the SSH to geoid height and in a next step to gravitational potential, information on the dynamic ocean topography (DOT) is required. For this purpose instantaneous DOT (iDOT) values derived from the profile approach [Bosch *et al.*, 2013] are used.

The spectral resolution of the measurements is 1 Hz corresponding to about 7 km along-track spatial resolution. The cross-track resolution strongly depends on the orbit of the dedicated mission and typically ranges between 300 km (TOPEX, Jason) and 80 km (ERS-1, Envisat). Only some missions use nonrepeat or long-repeat orbits (the so-called geodetic missions or geodetic mission phases, GM) with a cross-track separation of down to 8 km. A combination of different missions will further improve the spatial resolution. In our studies, data from ERS-1e/f GM phases (1994–1995), Envisat EM (end of live mission) phase (2010–2012), Jason-1 GM phase (2012–2013), and Cryosat (2010–2013) are used, allowing a mean spatial resolution of 10 km in the North Sea (dark green dots in Figure 1). Measurements close to coastlines are contaminated by land influences and thus are not reliable, so that for the Baltic Sea only sparse data are available. In order to account for range biases between different missions, we apply radial error corrections for each measurement derived from a multimission cross calibration [Bosch *et al.*, 2014].

2.5. Satellite Gravimetry

The ongoing and recently finished satellite missions GRACE (since 2002) and GOCE (2009–2013) are the main contributors to satellite gravimetry. The referring observations deliver valuable information in the long wavelengths and enable gravity field modeling approximately up to degree 150 (GRACE), i.e., spatial resolution at the Earth's surface of around 140 km and up to degree 250 (GOCE), respectively, around 80 km spatial resolution. Global SH satellite-only models, such as the GOCO series, enhance an optimum combination of GRACE and GOCE. The latest release GOCO05s [Mayer-Gürr *et al.*, 2015] is given with a spectral resolution up to degree and order (d/o) 280 and contains significant information at least up to degree 200, i.e., around 100 km spatial resolution. This global model serves in our study as prior information in order to deliver the low-resolution information. The observations of GRACE and GOCE are not directly introduced as regional data sets, as the extraction of local pieces from the satellite tracks according to the study area in Figure 1 does not allow resolving long wavelength information.

3. Regional Approach

Various geodetic techniques allow scanning the gravity field in different spectral domains. To achieve optimum modeling results, it is reasonable to use all available data, stemming from altimetry, terrestrial, airborne, shipborne, and satellite gravimetry. Our regional approach via spherical basis functions enables an efficient combination in selected areas where high-resolution data are available and further in the spectral domain where they contribute most information. As the different techniques observe different functionals of the gravity field, we have to specify respective observation equations. In the following we present the chosen tools and settings of our approach and give a kind of recipe for a reasonable parametrization. We enhance a balanced combination from the data sets of sections 2.1–2.4 and set up the estimation model at an appropriate level of discretization. We derive our approach from the relations of a global gravity field representation, due to the global support of our functions, which are defined as series expansions in terms of Legendre polynomials.

3.1. Tools and Settings

3.1.1. Spherical Basis Functions

It is well known that series expansions in terms of SBF are an appropriate tool for regional gravity field modeling [e.g., Freeden *et al.*, 1998; Schmidt *et al.*, 2007]. The functions are defined on a global scale, but they have highly localizing character which is adapted with profit for regional modeling approaches. In general, a SBF b is expressed by

$$b = b(\mathbf{x}, \mathbf{x}_q) = \sum_{l=0}^{\infty} \frac{2l+1}{4\pi} \left(\frac{R}{r}\right)^{l+1} B_l P_l(\mathbf{r}^T \mathbf{r}_q), \quad (1)$$

where $\mathbf{x} = r \cdot [\cos \varphi \cos \lambda, \cos \varphi \sin \lambda, \sin \varphi]^T = r \cdot \mathbf{r}$ means the geocentric position vector of a point $P(\lambda, \varphi, r)$ depending on longitude λ , latitude φ , and radial distance $r = |\mathbf{x}| = R + h'$; h' is the height of P over a sphere Ω_R with radius R ; \mathbf{r} denotes the unit vector. The position vector \mathbf{x}_q of the point $P(\lambda_q, \varphi_q, r_q) = P_q \in \Omega_R$ is defined analogously with $r_q = R$. Furthermore, in equation (1) P_l means the Legendre polynomial of degree l depending on the spherical distance angle $\theta_q = \arccos(\mathbf{r}^T \mathbf{r}_q)$ on the unit sphere; the Legendre coefficients B_l specify the shape of the SBF. In case of setting $B_l = 1$ for $l \in \mathbb{N}_0$, equation (1) defines the Abel-Poisson kernel.

Let the function $f = f(\lambda, \varphi, r) = f(\mathbf{x})$ be harmonic, it can be represented globally by the series expansion $f(\mathbf{x}) = \sum_{l=0}^{\infty} \sum_{m=-l}^l F_{l,m} H_{l,m}(\mathbf{x})$ in terms of solid SH functions $H_{l,m}(\mathbf{x})$ of degree l and order m . If $f(\mathbf{x})$ is given globally on the sphere Ω_R , i.e., $\mathbf{x} \in \Omega_R$, the SH coefficients $F_{l,m}$ can be determined uniquely.

In the sequel we deal with band-limited series expansions, truncated at the highest degree L in the spectral domain, i.e., $l = 0, 1, 2, \dots, L$. Herein the SH functions $H_{l,m}$ span the space $H_{0,\dots,L}(\Omega_R)$ of dimension $(L+1)^2$. [see Schmidt *et al.*, 2007]. If the set of basis functions (1) also spans the space $H_{0,\dots,L}(\Omega_R)$, they can be located on Q_L grid points $P_q \in \Omega_R$ with $q = 1, 2, \dots, Q_L$, and the corresponding Legendre coefficients B_l are restricted to $B_l = 0$ for $l > L$. Thus, the function $f \in H_{0,\dots,L}(\Omega_R)$ can alternatively be represented as series expansion

$$\begin{aligned} f = f(\mathbf{x}) &= \sum_{q=1}^{Q_L} d_q b(\mathbf{x}, \mathbf{x}_q) \\ &= \sum_{q=1}^{Q_L} d_q \sum_{l=0}^L \frac{2l+1}{4\pi} \left(\frac{R}{r}\right)^{l+1} B_l P_l(\mathbf{r}^T \mathbf{r}_q) . \end{aligned} \quad (2)$$

Consequently, the coefficients d_q are related to the SH coefficients $F_{l,m}$, and the reference to the Legendre polynomials P_l ensures the Laplace equation to be fulfilled. The estimation of the Q_L unknown coefficients d_q containing signal up to degree L is one of the key aspects of our modeling approach and is handled within an appropriate estimation model (cf. section 3.2).

3.1.2. Computation Grid and Global Rank Deficiency

In contrast to SH functions, the basis functions $b(\mathbf{x}, \mathbf{x}_q)$ from equation (1) are isotropic and centered in P_q . We use here a Reuter grid [Reuter, 1982] with an upper estimate of $N_{\max,L}^{\text{glob}} = 2 + \frac{4}{\pi} \gamma_L^2$ grid points in the global (glob) case [see Freeden *et al.*, 1998]. The equally distributed points of the computation grid guarantee a homogeneous coverage on a sphere Ω_R . Bentel *et al.* [2013b] tested several point grids in order to locate SBFs and showed that the differences between the resulting gravity models are marginal compared to the influence of other parameters, e.g., the choice of basis functions themselves (see section 3.1.7). The real global number $N_L^{\text{glob}} \leq N_{\max,L}^{\text{glob}}$ of grid points corresponds to the global number Q_L^{glob} of unknown coefficients which have to be estimated in the analysis step (see section 3.2.1). For $Q_L^{\text{glob}} = (L+1)^2$ the point system becomes fundamental, and the normal equations can be solved, as it is handled in global gravity field representations using SHs.

However, as the SBFs are located on a computation grid, the number Q_L^{glob} of coefficients usually exceeds the dimension of the space $H_{0,\dots,L}(\Omega_R)$. Thus, the transformation equation from the $(L+1)^2$ SHs $H_{l,m}(\mathbf{x})$ into the Q_L^{glob} SBFs $b(\mathbf{x}, \mathbf{x}_q)$ contains $Q_L^{\text{glob}} - (L+1)^2$ linear dependencies between the basis functions, quoting the global rank deficiency $k_L^{\text{glob}} = Q_L^{\text{glob}} - (L+1)^2$. Respectively, we chose the number $Q_L^{\text{glob}} = N_L^{\text{glob}}$ of coefficients, i.e., the real number of grid points of the Reuter grid, with $(L+1)^2 \leq Q_L^{\text{glob}} \leq N_{\max,L}^{\text{glob}}$, to ensure both, covering the frequency domain up to L and minimizing k_L^{glob} .

Consequently, we derive the characteristic control parameter γ_L of the Reuter grid as a resolution-dependent parameter for the maximum degree L (highest spectral resolution, respectively). Following the above considerations, we choose

$$\gamma_L^2 = (L+1)^2 \quad (3)$$

from $(L+1)^2 \leq 2 + \frac{4}{\pi} \gamma_L^2$, assuming $\frac{4}{\pi} \approx 1$ and neglecting the additional value of 2. Thus, the number of grid points increases with a rising maximum resolution L . The higher the resolution L , the denser the grid, the more SBFs are placed in the computation grid, the sharper is their peak in the spatial domain, and thus, the more details can be modeled.

In the following we transfer these investigations from global to regional settings.

3.1.3. Definition of Regional Target, Observation, and Computation Area

In contrast to global applications, we have to care about several challenges in the regional case—discussed in the following sections—first of all the choice of the extension of the region, depending on the given observations. Vice versa, for a given task in a specific area we would have to select appropriate and available data sets. In this paper we focus on the first case, as our aim is to extract the maximum gravitational information from different given measurements. Consequently, we have to set up the estimation model such that it fits the data as optimally as possible. In our approach, we distinguish first a computation area $\partial\Omega_C \subset \Omega_R$ to locate the previous introduced basis functions $b(\mathbf{x}, \mathbf{x}_q)$, equation (1), at the Reuter grid points P_q (cf. section 3.1.2), second an observation area $\partial\Omega_O$, i.e., the area in which we project the given observations, and third the area

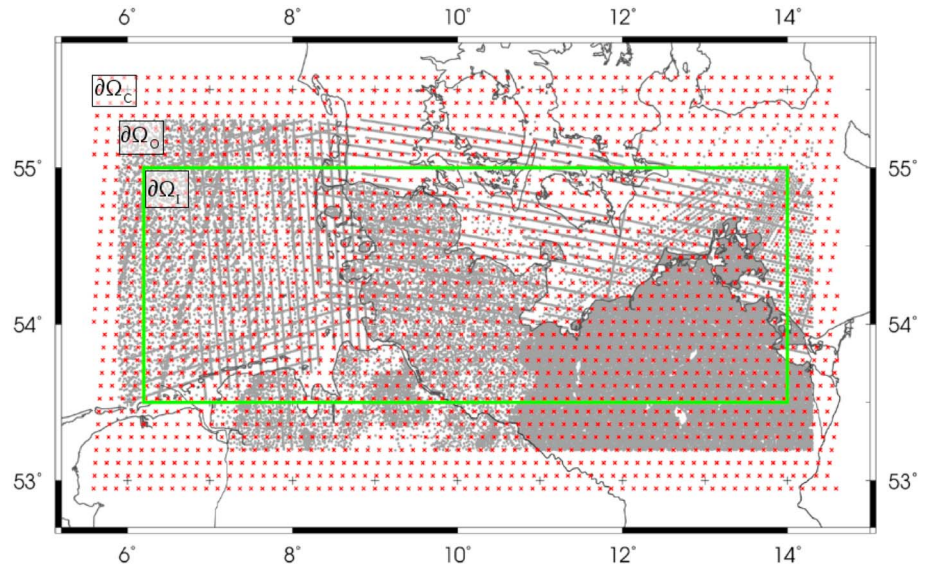


Figure 2. Study region in Northern Germany: the green bordered area defines the area of investigation $\partial\Omega_i$; the gray lines represent the measurement sites within the observation area $\partial\Omega_o$. The red crosses mark the Reuter grid points P_q within the computation area $\partial\Omega_c$ (regional number $Q_L = 2118$, $L = 2190$). The margins between the areas amount each around 0.3° (for $J = 11$).

of investigation $\partial\Omega_i$, i.e., the target area of the final output gravity model. The three areas have different extensions, resulting on the one hand from the restriction of the global functions to a specific region; to avoid artificial structures stemming from side lobes of the SBFs, we have to choose $\partial\Omega_c$ as the largest area and thus $\partial\Omega_o \subset \partial\Omega_c$. On the other hand, the corresponding coefficients d_q can only be estimated properly if their locations are covered by observations in a certain surrounding zone of influence. Thus, missing observations lead to insufficiently estimated coefficients and provoke edge effects so that we further have to choose $\partial\Omega_i \subset \partial\Omega_o$. For a practicable implementation, the size of the resolution-depending margins is coupled on the choice of the basis functions. We discuss the relation in section 3.1.5.

From the coverage of all available data sets, we choose $\partial\Omega_o$ and then adapt $\partial\Omega_c$ and $\partial\Omega_i$ with equal margins. For our study region in Northern Germany, described in section 2, the extensions of the three areas are depicted in Figure 2.

3.1.4. Estimate of the Regional Rank Deficiency

For partial computation areas $\partial\Omega_c$ the regional rank deficiency k_L^{reg} is assumed to be proportional to the global rank deficiency k_L^{glob} , in the same measure as the surface ratio $\partial\Omega_c/\Omega_R$ and the ratio of computation points Q_L/Q_L^{glob} . We estimate the regional rank deficiency, related to the initial guess of the rank by Naeimi [2013], with

$$k_L^{\text{reg}} \cong \frac{\partial\Omega_c}{\Omega_R} \left[Q_L^{\text{glob}} - (L+1)^2 \right]. \quad (4)$$

Equation (4) depends on the resolution L and the extension of the target area. Hereby, k_L^{reg} describes linear dependencies between the basis functions, according to k_L^{glob} (see section 3.1.2). We minimize the regional rank deficiency problem by the choice of an appropriate maximum degree L of the approach (see section 3.1.6). Additional rank deficiency problems might appear due to inhomogeneous data distribution, whose reduction is discussed in section 3.2.

3.1.5. Discretization of the Frequency Spectrum

The consistent combination of the different observation techniques requires a rougher discretization of the frequency domain than by degree l in order to classify the different techniques with respect to their spectral resolution. We choose the so-called resolution levels

$$j = \lfloor \log_2 (l_j + 1) \rfloor. \quad (5)$$

to define frequency bands by a level-depending maximum degree $l_j = 2^j - 1$ of appropriate series expansions over degree l . Figure 3 shows a general concept of discretizing the frequency spectrum and the attribution

j	1	2	3	4	5	6	7	8	9	10	11	12	...
l_j [deg]	1	3	7	15	31	63	127	255	511	1023	2047	4095	...
$\rho_{\max,j}$ [km]	20000	6667	2857	1333	645	317	157	78	39	20	10	5	...
resolution	satellite gravimetry												
											altimetry		
											terrestrial, air-/shipborne gravimetry		

Figure 3. Extract of the frequency domain which is split into several resolution levels j . Each level is related to a maximum degree l_j of a series expansion and a maximum spatial resolution $\rho_{\max,j}$. The different observation techniques are attributed to the classification by their spectral resolution: low (satellite gravimetry data in yellow), middle (altimetry in green), and high (airborne, shipborne and terrestrial gravimetry in orange). In our specific test area, the mean resolution of the altimetry, shipborne, airborne, and terrestrial data corresponds to level $j = 11$ (red bordered).

of the different observation techniques to the resolution levels j depending on their spectral and spatial resolution. $\rho_{\max,j}$ is the according maximum spatial resolution for one level j from the averaged relationship $l_j \leq (\pi R)/(\rho_{\max,j})$ on a sphere with radius R . We derive $\rho_{\max,j}$ approximately from $(\pi R)/l_j \geq \rho_{\max,j}$ to reproduce the Nyquist theorem. The achievable maximum level $j = J$ depends on the maximum degree l_j and thus on the maximum spatial resolution $\rho_{\max,J}$ of the observations.

The base 2 in equation (5) specifies the range of the frequency bands. The choice is appropriate for the flexible combination of different observation types: typical measurement systems achieve $L \approx 4000$ for high-resolution terrestrial and airborne observations, $L \approx 2000$ for middle-resolution altimetry data, and $L \approx 250, 120, 60, \dots$ for low-resolution satellite measurements. In our study, the exemplarily chosen test area Northern Germany is well observed by high- and middle-resolution data (see Figure 1). As long wavelengths cannot be resolved in this spatially limited area (according to the Nyquist theorem), satellite gravimetry information is introduced as prior information (see section 3.2) in terms of the global SH model GOCO05s (section 2.5).

The adaptation of the resolution levels by a base different from 2 may be suitable for modeling approaches using only one technique in order to extract the highest measure of information, see studies in Schmidt *et al.* [2007]. According to the level-depending fragmentation of the frequency spectrum, a MRR—also known as multiscale representation—can be applied. [see, e.g., Freeden, 1999; Freeden and Michel, 2001; Schmidt *et al.*, 2007]. However, these issues will not be discussed in this paper.

3.1.6. Choice of the Modeling Resolution

From the generalized spectral attribution of the data to the frequency spectrum in Figure 3 and their actual spatial resolution in the specific cases, we derive both a minimum and maximum modeling resolution, l' and L . The highest resolution level J with l_j is adapted to the spectral content of the observations, such that $l_j \leq L$: The maximum modeling resolution L is chosen higher, on the one hand, to minimize omission errors stemming from the truncation of the infinite series expansion equation (1) and, on the other hand, to minimize the previous discussed rank deficiency k_L^{reg} , equation (4), so that $l_j \leq L \leq L^{\text{rank}}$. In the ideal case, $k_L^{\text{reg}} =: k_{l_j}^{\text{reg}}$ becomes 0. Following this assumption, we set $Q_{l_j}^{\text{glob}} - (L^{\text{rank}} + 1)^2 = 0$ (cf. section 3.1.4) with $Q_L^{\text{glob}} = Q_{l_j}^{\text{glob}}$ and $l_j = L^{\text{rank}}$ and obtain an upper estimate

$$L^{\text{rank}} = \left\lceil \sqrt{Q_{l_j}^{\text{glob}}} - 1 \right\rceil, \quad (6)$$

rounded down to the next natural number. L^{rank} depends on the size of the computation area $\partial\Omega_C$ and thus on the maximum number $Q_{l_j}^{\text{glob}}$ of corresponding Reuter grid points.

3.1.7. Choice of the Basis Function

In order to extract the specific frequency domains for gravity field modeling approaches, we relate the band-limiting basis functions $b(\mathbf{x}, \mathbf{x}_q)$ from equation (2) to the resolution levels j , acting as low-pass filters up to the cutoff frequency l_j . We deal with the following two examples [see Schmidt *et al.*, 2007]:

1. *Shannon function.* The Legendre coefficients B_l are defined as

$$B_l = \begin{cases} 1 & \text{for } l = 0, \dots, 2^j - 1 \\ 0 & \text{for } l \geq 2^j \end{cases} =: B_{j,l}^{\text{Sh}}. \quad (7)$$

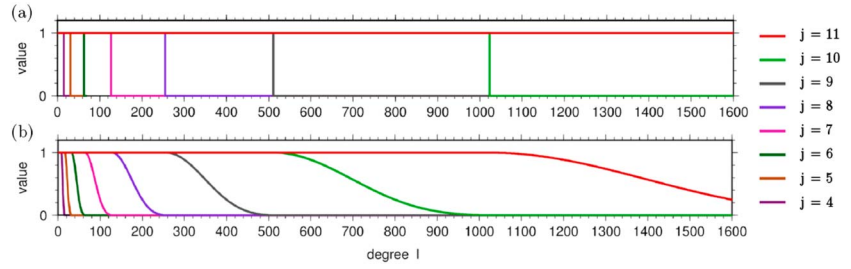


Figure 4. Legendre coefficients B_l of the (a) Shannon and (b) Blackman scaling function for different resolution levels j ; spectral representation.

2. *Blackman function.* The Legendre coefficients B_l are defined as

$$B_l = \begin{cases} 1 & \text{for } l = 0, \dots, 2^{j-1} - 1 \\ A_j(l) & \text{for } l = 2^{j-1}, \dots, 2^j - 1 \\ 0 & \text{for } l \geq 2^j \end{cases} =: B_{j,l}^{\text{Bl}}. \quad (8)$$

The Blackman function is based on the Blackman window

$$A_j(l) = \frac{21}{50} - \frac{1}{2} \cos\left(\frac{2\pi l}{2^j}\right) + \frac{2}{25} \cos\left(\frac{4\pi l}{2^j}\right),$$

which is often used in classical signal analysis.

Figure 4 visualizes the Legendre coefficients B_l of (a) the Shannon function (7) and (b) the Blackman function (8), for selected levels $j = 4, \dots, 11$ in an extract of the frequency domain. In each case the panel shows the spectral performance depending on the degree l . Whereas the Shannon function declines exactly at the upper boundary of each resolution level, i.e., at the cutoff frequency l_j , from 1 to 0 and thus features a jump discontinuity, the Blackman function decreases smoothly in-between $l_{j-1} \dots l_j$. The sharper the cut in the frequency domain, the larger are oscillations in the spatial domain. Those overlapping side lobes might cause artificial effects on the modeling results of neighboring basis functions (cf. section 3.1.3). Consequently, Blackman scaling functions are a good compromise between a moderate declining behavior, i.e., loss of signal, in the spectral domain, but only weak oscillations in the spatial domain. Further, the higher the level, the sharper the peak of a function, the less comprehensive the oscillations. Besides the Shannon and Blackman functions many other appropriate basis functions exist; *Bentel et al.* [2013a] and *Bentel et al.* [2013b] present a catalog of basis functions and studied their main features in detail. (In the aforementioned references, the Blackman function is defined in a slightly different way than in equation (8).)

3.1.8. Choice of Area Margins

From all basis functions, the Shannon function has the strongest spatial oscillations due to its exact band limitation in the frequency domain (cf. section 3.1.7). Taking these resolution-depending side lobes into account, we derive the margins between the different areas, mentioned in section 3.1.3. According to our investigations and as a rule of thumb, we set the width $\eta'_{O,C}$ of the margin between the observation area $\partial\Omega_O$ and the computation area $\partial\Omega_C$ equal to the width $\eta'_{I,O}$ of the margin between the target area $\partial\Omega_I$ and the observation area $\partial\Omega_O$:

$$\eta' = \eta'_{I,O} = \eta'_{O,C} = \frac{180^\circ}{2^{J-1} \cos(|\varphi|_{\max})}. \quad (9)$$

Thus, the extension of the margins depends on the chosen maximum resolution level J and the maximum absolute value $|\varphi|_{\max}$ of the latitude of $\partial\Omega_I$.

3.2. Estimation Model

Based on the fundamentals derived in the previous section 3.1, we set up an estimation model in order to compute regional gravity fields at any resolution level j from the combination of appropriate input data. In the general procedure of our approach we identify the function f with the difference ΔV between the gravitational potential V of the Earth and the gravitational potential V_{back} of a given global background model, i.e.,

$$f = f(\mathbf{x}) = \Delta V(\mathbf{x}) = V(\mathbf{x}) - V_{\text{back}}(\mathbf{x}). \quad (10)$$

The global background model covers the low frequencies, as the appropriate long wavelengths cannot be estimated by regional approaches on the one hand, and on the other hand, they are already very well approximated in existing global models.

The Earth's gravity field is monitored from different geodetic observation techniques by measuring various functionals $\mathcal{Y}[V]$ of the gravitational potential V , e.g., gravity anomalies Dg , disturbances δg , or gradients V_{ab} ($a, b \in \{x, y, z\}$). We adapt the basis function $b(\mathbf{x}, \mathbf{x}_q)$ from equation (2), describing the gravitational potential V , to the corresponding functionals $\mathcal{Y}[V]$ and denote it as $\tilde{b}(\mathbf{x}, \mathbf{x}_q)$. Introducing the measurement error e , the observation equation for one observation site $P(\mathbf{x}^p)$ ($p = 1, \dots, n$) follows from equation (2) with $\mathbf{x} = \mathbf{x}^p$ and reads with $\mathcal{Y}[V(\mathbf{x}^p)] - \mathcal{Y}[V_{\text{back}}(\mathbf{x}^p)] =: y(\mathbf{x}^p)$

$$y(\mathbf{x}^p) + e(\mathbf{x}^p) = \sum_{q=1}^{Q_L} d_q \tilde{b}(\mathbf{x}^p, \mathbf{x}_q). \quad (11)$$

For the estimation of the unknown scaling coefficient vector $\mathbf{d}_L = [d_1, \dots, d_{Q_L}]^T$, we collect the observations $y(\mathbf{x}^p)$ in the $n \times 1$ observation vector \mathbf{y} and set up a linear adjustment model. We use here the *Gauss-Markov model* (GMM)

$$\mathbf{y} + \mathbf{e} = \mathbf{A} \mathbf{d}_L \quad \text{with} \quad D(\mathbf{y}) = \sigma^2 \mathbf{P}^{-1}. \quad (12)$$

In the deterministic part, $\mathbf{e} = [e(\mathbf{x}^1), \dots, e(\mathbf{x}^p)]^T$ is the $n \times 1$ vector of the measurement errors, and $\mathbf{A} = [\tilde{b}(\mathbf{x}^p, \mathbf{x}_q)]$ is the $n \times Q_L$ design matrix, containing the appropriate basis functions $\tilde{b}(\mathbf{x}^p, \mathbf{x}_q)$. (The coefficients \mathbf{d}_L have the SI unit m^2/s^2 of the gravitational potential; the elements of the design matrix \mathbf{A} contain the corresponding conversion factors for the particular functionals.) In the stochastic part, i.e., the right-hand equation in (12), σ^2 is the unknown variance factor, and \mathbf{P} is the $n \times n$ given positive definite weight matrix of the observation vector \mathbf{y} . Due to the linear dependencies between the spherical basis functions, the regional rank deficiency of matrix \mathbf{A} can be approximated by equation (4) (cf. section 3.1.4). Besides this rank deficiency problem, the normal equation system—following from the application of the least squares method to the GMM (12)—might be ill conditioned due to downward continuation problems and data gaps. To overcome these three problems, we additionally introduce the linear model

$$\boldsymbol{\mu}_d + \mathbf{e}_d = \mathbf{d}_L \quad \text{with} \quad D(\boldsymbol{\mu}_d) = \sigma_d^2 \mathbf{P}_d^{-1} \quad (13)$$

as prior information. In equation (13), $\boldsymbol{\mu}_d$ and \mathbf{P}_d^{-1} are the given $Q_L \times 1$ expectation vector and the given $Q_L \times Q_L$ covariance matrix of the vector \mathbf{d}_L of the series coefficients. \mathbf{e}_d and σ_d^2 are the unknown error vector and the unknown variance factor of the prior information. The combination of the two linear models (12) and (13) yields a unique solution [see, e.g., Schmidt et al., 2007].

3.2.1. Analysis: Estimation of Coefficients

In the analysis step we use the Shannon function in order to set up the estimation model for the determination of the unknown series coefficients \mathbf{d}_L . According to section 3.1.7 and Figure 4a, this kernel with referring Legendre coefficients $B_{j,l}^{\text{Sh}}$ (7) ensures to keep full signal content for the series coefficients \mathbf{d}_L up to the cutoff frequency, here $L \geq l_j$ (cf. section 3.1.6). The coefficients represent in the spatial domain the height of the basis functions. As already mentioned, they are point parameters belonging to altogether Q_L grid points $P_q \in \partial\Omega_C$.

For the different observed functionals $\mathcal{Y}[V]$ of the Earth's gravity field, we have to formulate different observation equations (11): We adapt the general expression of the basis function $b(\mathbf{x}, \mathbf{x}_q)$ in equation (2) with $\mathbf{x} = \mathbf{x}^p$ and $B_l = B_{j,l}^{\text{Sh}}$ (7). Table 1 exemplarily lists modified basis functions $b(\mathbf{x}^p, \mathbf{x}_q) = \tilde{b}(\mathbf{x}^p, \mathbf{x}_q)$ for different functionals $\mathcal{Y}[V] \in \{\Delta V, V_{zz}, T, Dg, \delta g, \dots\}$, with ΔV potential differences obtained from GRACE (the GRACE satellite mission delivers potential differences ΔV from observations at different observation sites $P(\mathbf{x}^{i,p}), P(\mathbf{x}^{ii,p})$ of the two GRACE satellites i, ii), V_{zz} second derivatives of V (exemplarily for one of the six gradients of the GOCE mission), T disturbing potential derived from altimetric SSH measurements (we relate the geoid heights $N = (\text{SSH} - \text{DOT})$ after Bruns equation $N = T/\gamma$ to the disturbing potential and the normal gravity γ at the ellipsoid), Dg gravity anomalies, and δg gravity disturbances, both mainly obtained from terrestrial, airborne, or shipborne measurements. According to the data sets in section 2, we apply in the following the relations $\mathcal{Y}[V] = T, Dg, \delta g$.

For the combination of different observation techniques, we extend the parameter estimation model (12): Let \mathbf{y}_k with $k = 1, \dots, K$ be the $n_k \times 1$ observation vector of the k^{th} measurement technique, \mathbf{e}_k and \mathbf{A}_k the corresponding $n_k \times 1$ error vector and the $n_k \times Q_L$ design matrix. The model for combining altogether K observation

Table 1. Selection of Adapted Basis Functions $\tilde{b} = \tilde{b}(\mathbf{x}, \mathbf{x}_q)$ for (1) Formulating Observation Equations From Gravity Functionals $\mathcal{Y}[V]$, Observed at Locations $\mathbf{x} = \mathbf{x}^p$ in the Analysis and (2) Computing Output Functionals at Locations $\mathbf{x} = \mathbf{x}^c$ in the Synthesis^a

Observation Technique	Functional $\mathcal{Y}[V]$	Adapted Basis Function \tilde{b}
GRACE	ΔV	$\tilde{b}(\mathbf{x}^i, \mathbf{x}_q) = \sum_{l=0}^L \frac{2l+1}{4\pi} \left[\left(\frac{R}{r} \right)^{l+1} B_l P_l(\cos\theta_q^i) - \left(\frac{R}{r^i} \right)^{l+1} B_l P_l(\cos\theta_q^i) \right]$
GOCE	V_{zz}	$\tilde{b}(\mathbf{x}, \mathbf{x}_q) = \sum_{l=0}^L \frac{2l+1}{4\pi} \frac{(l+1)(l+2)}{r^2} \left(\frac{R}{r} \right)^{l+1} B_l P_l(\cos\theta_q)$
Altimetry	$T = (\text{SSH} - \text{DOT})_T$	$\tilde{b}(\mathbf{x}, \mathbf{x}_q) = \sum_{l=0}^L \frac{2l+1}{4\pi} \left(\frac{R}{r} \right)^{l+1} B_l P_l(\cos\theta_q)$
Shipborne, airborne and	Dg	$\tilde{b}(\mathbf{x}, \mathbf{x}_q) = \sum_{l=0}^L \frac{2l+1}{4\pi} \frac{l-1}{r} \left(\frac{R}{r} \right)^{l+1} B_l P_l(\cos\theta_q)$
terrestrial gravimetry	δg	$\tilde{b}(\mathbf{x}, \mathbf{x}_q) = \sum_{l=0}^L \frac{2l+1}{4\pi} \frac{1-l}{r} \left(\frac{R}{r} \right)^{l+1} B_l P_l(\cos\theta_q)$

^aThe vertical arrangement follows the spectral classification of the observation techniques in Figure 3 from low up to high resolution.

techniques then reads

$$\begin{bmatrix} \mathbf{y}_1 \\ \mathbf{y}_2 \\ \vdots \\ \mathbf{y}_K \\ \boldsymbol{\mu}_d \end{bmatrix} + \begin{bmatrix} \mathbf{e}_1 \\ \mathbf{e}_2 \\ \vdots \\ \mathbf{e}_K \\ \mathbf{e}_d \end{bmatrix} = \begin{bmatrix} \mathbf{A}_1 \\ \mathbf{A}_2 \\ \vdots \\ \mathbf{A}_K \\ \mathbf{I} \end{bmatrix} \mathbf{d}_L$$

with

$$D \begin{bmatrix} \mathbf{y}_1 \\ \mathbf{y}_2 \\ \vdots \\ \mathbf{y}_K \\ \boldsymbol{\mu}_d \end{bmatrix} = \begin{bmatrix} \sigma_1^2 \mathbf{P}_1^{-1} & \mathbf{0} & \dots & \mathbf{0} & \mathbf{0} \\ \mathbf{0} & \sigma_2^2 \mathbf{P}_2^{-1} & \dots & \mathbf{0} & \mathbf{0} \\ \vdots & \vdots & \ddots & \vdots & \vdots \\ \mathbf{0} & \mathbf{0} & \dots & \sigma_K^2 \mathbf{P}_K^{-1} & \mathbf{0} \\ \mathbf{0} & \mathbf{0} & \dots & \mathbf{0} & \sigma_d^2 \mathbf{P}_d^{-1} \end{bmatrix} \quad (14)$$

where we included the additional model (13) for the prior information [see *Schmidt et al.*, 2015]. Further, the covariance block matrices $D(\mathbf{y}_k) = \sigma_k^2 \mathbf{P}_k^{-1}$ consist each of a given $n_k \times n_k$ positive definite weight matrix \mathbf{P}_k and an unknown variance factor σ_k^2 . The matrices \mathbf{P}_k are located on the main diagonal of the full covariance matrix from equation (14); the nondiagonal block matrices are zero matrices, assuming that the observation groups \mathbf{y}_k are uncorrelated. A combination on observation equation level would capture the information of each observation technique most comprehensively and deliver instantly residuals of the observations. Because of the size and thus the computation time of the linear equation systems, we combine the observation techniques on normal equation level. Consequently, the system is independent from the number of observations, and the residuals of the observations have to be derived separately, but we obtain however the full covariance information of the unknowns. We apply the method of VCE to the GMM (14), yielding the normal equation system

$$\left(\sum_{k=1}^K \left(\frac{1}{\sigma_k^2} \mathbf{A}_k^T \mathbf{P}_k \mathbf{A}_k \right) + \frac{1}{\sigma_d^2} \mathbf{P}_d \right) \hat{\mathbf{d}}_L = \sum_{k=1}^K \left(\frac{1}{\sigma_k^2} \mathbf{A}_k^T \mathbf{P}_k \mathbf{y}_k \right) + \frac{1}{\sigma_d^2} \mathbf{P}_d \boldsymbol{\mu}_d. \quad (15)$$

The estimator $\hat{\mathbf{d}}_L$ reads for the development of the series expansion up to resolution L in the point of convergence

$$\hat{\mathbf{d}}_L = \left(\sum_{k=1}^K \left(\frac{1}{\hat{\sigma}_k^2} \mathbf{A}_k^T \mathbf{P}_k \mathbf{A}_k \right) + \frac{1}{\hat{\sigma}_d^2} \mathbf{P}_d \right)^{-1} \left(\sum_{k=1}^K \left(\frac{1}{\hat{\sigma}_k^2} \mathbf{A}_k^T \mathbf{P}_k \mathbf{y}_k \right) + \frac{1}{\hat{\sigma}_d^2} \mathbf{P}_d \boldsymbol{\mu}_d \right) \quad (16)$$

[see, e.g., *Koch and Kusche*, 2002]. Hereby, the reciprocal of the square of the iteratively computed variance components (VC) $\hat{\sigma}_k^2$ and $\hat{\sigma}_d^2$ determines the relative weight of each observation group \mathbf{y}_k and of the prior information $\boldsymbol{\mu}_d$. Thus, the contribution of each observation technique to the overall combination result is regulated and depends on the measurement accuracy, but also on the number, the spectral resolution, and the spatial distribution of the data. The latter issue plays a very important role for the contribution of the prior

information μ_d , adjusted by σ_d^2 . This weight becomes larger in case of data gaps. We discuss the application and the behavior with real data in section 4.2.

The precision of the estimated coefficients $\hat{\mathbf{d}}_L$ in equation (16) can be evaluated by applying the law of error propagation, resulting in the covariance matrix

$$D(\hat{\mathbf{d}}_L) = \mathbf{Q}_{dd}^{-1} = \begin{bmatrix} v(\hat{d}_1) & c(\hat{d}_1, \hat{d}_2) & \dots & c(\hat{d}_1, \hat{d}_{Q_L}) \\ c(\hat{d}_2, \hat{d}_1) & v(\hat{d}_2) & & \vdots \\ \vdots & & \ddots & \\ c(\hat{d}_{Q_L}, \hat{d}_1) & \dots & & v(\hat{d}_{Q_L}) \end{bmatrix}^{-1}. \quad (17)$$

\mathbf{Q}_{dd} is the $Q_L \times Q_L$ normal equation matrix as defined in equation (15), left side, and inverted in equation (16). The main diagonal contains the variances $v(\hat{d}_q)$ of the estimated coefficients $\hat{\mathbf{d}}_L$, while the other elements represent the covariances, e.g., $c(\hat{d}_1, \hat{d}_2)$, between two coefficients.

3.2.2. Synthesis: Computation of Gravity Field Functionals

In order to express different functionals of the Earth's gravity field in specific regions, we use the vector $\hat{\mathbf{d}}_L$ of estimated coefficients from equation (16) and multiply it with adapted basis functions $\tilde{b}(\mathbf{x}^c, \mathbf{x}_q)$. As we apply the Shannon kernel without any smoothing behavior in the analysis, we are now, in the synthesis, able to multiply the coefficients with different kernel functions following Schreiner [1996]. We develop series expansions in terms of low-pass filtering Blackman scaling functions, setting $B_l = B_{jl}^{\text{Bl}}$ according to equation (8) and thus profit from the reduction of erroneous side lobes in the spatial domain (cf. section 3.1.7 and see Schmidt et al. [2007] and Bentel et al. [2013a]). $\tilde{b}(\mathbf{x}^c, \mathbf{x}_q)$ are expressed by the relations from Table 1, analogous to the analysis, cf. section 3.2.1. The functionals can be complemented, e.g., by quasi-geoid heights ζ , deflections of the vertical (ξ, η), or equivalent water heights. The values are now computed at locations \mathbf{x}^c with $c = 1, \dots, C$ points $P(\mathbf{x}^c)$ inside the target area $\partial\Omega$, e.g., on selected points, on a regular grid or along flight tracks, in any height above the Earth's surface. For any functional $z(\mathbf{x}^c)$ the equation system of the synthesis then reads

$$\mathbf{z} = \mathbf{B} \hat{\mathbf{d}}_L \quad (18)$$

with $\mathbf{z} = [z(\mathbf{x}^c)]$ and $\mathbf{B} = [\tilde{b}(\mathbf{x}^c, \mathbf{x}_q)]$.

3.2.3. Error Propagation

In order to derive information about the precision and the dependencies of the resulting functionals (18), we compute their variances and covariances at the output grid points $P(\mathbf{x}^c)$ by applying the law of error propagation. For one functional $z(\mathbf{x}^c)$ in (18) the full covariance matrix $D(\mathbf{z})$ of size $C \times C$ can be expressed by

$$D(\mathbf{z}) = \mathbf{B} D(\hat{\mathbf{d}}_L) \mathbf{B}^T. \quad (19)$$

Thus, the covariance matrix

$$D(\mathbf{z}) = \begin{bmatrix} v(z(\mathbf{x}^1)) & c(z(\mathbf{x}^1, \mathbf{x}^2)) & \dots & c(z(\mathbf{x}^1, \mathbf{x}^C)) \\ c(z(\mathbf{x}^2, \mathbf{x}^1)) & v(z(\mathbf{x}^2)) & & \vdots \\ \vdots & & \ddots & \\ c(z(\mathbf{x}^C, \mathbf{x}^1)) & \dots & & v(z(\mathbf{x}^C)) \end{bmatrix} \quad (20)$$

contains on the main diagonal the variances $v(z(\mathbf{x}^c))$, indicating the precision of the modeling result. The other elements represent the covariances $c(z(\mathbf{x}^1, \mathbf{x}^2))$ between two values at, e.g., the output grid points $P(\mathbf{x}^1)$ and $P(\mathbf{x}^2)$, including a measure for the dependency between the first and the second point.

4. Computation, Results, and Validation

4.1. Setting Up the Approach

Following the regional gravity modeling specifications in section 3, we model gravitational structures in our study area in Northern Germany from the combination of the different data sets, introduced in sections 2.1–2.4. All observations are reduced by the SH background model $V_{\text{back}}(\mathbf{x}^p)$ (cf. equation (10)) GOCO05s (cf. section 2.5) up to degree $l = 127$ according to the level restriction of $j = 7$ (cf. Figure 3), in order to remove potential long wavelengths from the regional data sets. The mean spatial resolution of the observations counts 10 km for the whole area. Consequently, we set up our approach at level $J = 11$ (cf. Figure 3,

Table 2. Order of Magnitude of the Estimated VCs for Each Observation Group k and the Prior Information, Referenced to Group [1] With Highest Relative Weight, Thus Smallest VC

Observation Group k	Observation Type	Data Set	Relative Weight
[1]	terrestrial	BKG	1
[2]	airborne	North Sea	1
[3]	airborne	Baltic Sea	1
[4]	shipborne	BKG	10^{-1}
[5]	altimetry	ERS-1e	10^{-3}
[6]	altimetry	ERS-1f	10^{-3}
[7]	altimetry	Cryosat RADS	10^{-3}
[8]	altimetry	Envisat EM	10^{-3}
[9]	altimetry	Jason-1 GM	10^{-3}
	prior information	GOCO05s	10^{-5}

red bordered): In the analysis (section 3.2.1), we develop the series expansion up to a maximum resolution of $L = 2190$, i.e., a value between $l_j = 2047$ and $L^{\text{rank}} = 2310$, equation (6), cf. section 3.1.6, in analogy to the maximum degree of the global SH model EGM2008. It is smoothed down to degree $l_j = l_{11} = 2047$ in the synthesis (section 3.2.2). The level-dependent margins (9) between target, observation, and computation area result in $\eta_{l,0}^{11} = \eta_{0,c}^{11} = 0.3^\circ$ with $|\varphi|_{\max} = 55^\circ$ and $J = 11$ (cf. Figure 2). Since the computation area $\partial\Omega_c$ consists of $N_L = 2118$ Reuter grid points, $Q_L = Q_{2190} = 2118$ unknown coefficients d_q have to be determined (cf. 3.1.3).

The estimation model (14) contains the functional relationships for the $K = 9$ different observation groups from terrestrial [1], airborne (two campaigns: North Sea [2] and Baltic Sea [3]), and shipborne [4] gravimetry, as well as from altimetry (missions: ERS-1e [5], ERS-1f [6], Cryosat [7], Envisat EM [8], and Jason-1 GM [9]), see Table 1. As prior information we introduce the same global SH model as the subtracted background model GOCO05s up to $l = 127$, contributing low-resolution information mainly stemming from satellite gravimetry (cf. section 2.5). Thus, the expectation value can be set to $\mu_d = \mathbf{0}$ and $\Sigma_d = \mathbf{I}$ (identity matrix), assuming the SH model as noise free. We further treat all $K = 9$ groups as independent data sets. Both, due to the variety of different measurement systems and due to the unrelated observation time spans, it is justified to neglect the correlations between the observation groups k , cf. section 3.2.1 and equation (14). Further, we introduce identity matrices $\mathbf{P}_k = \mathbf{I}$, assuming no correlations and similar accuracies of the measurements \mathbf{y}_k of one data type, due to insufficient information about the data quality and due to considerably smaller computational expense.

4.2. Relative Weighting of Data Sets

The estimated VCs indicate the relative weighting of the different observation groups and thus their contribution to the resulting model depending on the quality and the quantity of the input data. Table 2 lists the relative weights $\hat{\sigma}_k^{-2}$, i.e., the reciprocal of the VCs, for all observation groups k referred to the observation group [1] ($k = 1$). This terrestrial data set obtains the smallest VC, i.e., the highest relative weight due to several positive features, such as high data quality and quantity: the observations show a good signal-to-noise (S/N) ratio, few data gaps, homogeneous and widespread distribution, and high spectral resolution (cf. section 2.1). (Initial values for the iteration of the VCs are set to $\sigma_k = \sigma_d = 0.001$, so that the number of iteration steps averages between 10 and 15. The stop criterion is reached if the values do not change up to the second decimal place. These empirical values optimize the computation time.)

The offshore shipborne measurements [4] are downweighted relatively to [1] by 1 order of magnitude, due to their spatial limitation and lower accuracy (cf. section 2.3). The downward continuation of the airborne measurements [2] and [3] may reduce their s/n ratio as well, but the effect is marginal so that [2] and [3] get the same high relative weights as [1].

The altimetry measurements [5] to [9] get each similar weights, but they are downweighted 3 orders of magnitude compared to [1]: Especially the limited spatial resolution (cf. section 2.4) reduces their signal content and contribution to the combined solution here; the low influence in contrast to [4] probably stems from the strong preprocessing of the originally less accurate shipborne data.

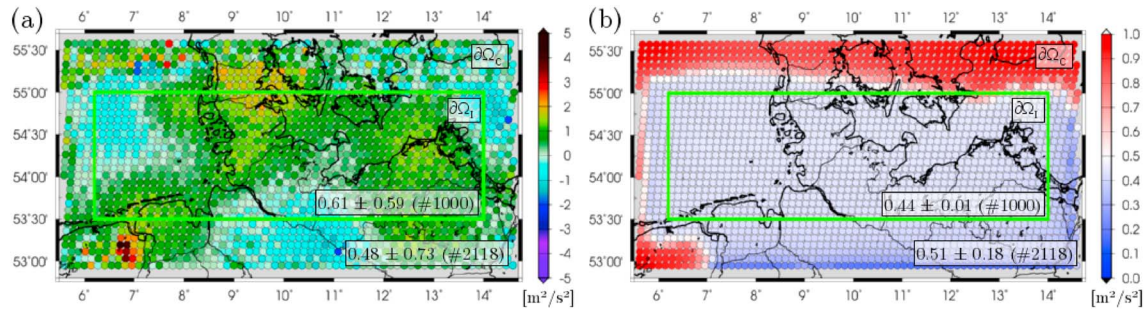


Figure 5. (a) Estimated coefficients \hat{d}_L and their (b) standard deviations σ_d up to $L = 2190$ within the computation area $\partial\Omega_C$. The area of investigation $\partial\Omega_I$ is bordered in green. For each area the mean value and its standard deviation (of the 2118, 1000 coefficients) are displayed in the boxes. All numbers are given in m^2/s^2 after scaling the design matrices \mathbf{A}_k and reducing the observations by a mean value.

The impact of the prior information μ_d is very weak, indicated by a 5 times lower weight compared with the terrestrial data [1]. As in general, the target area is well observed by high- and middle-resolution measurement systems, there is only little need for filling in data gaps, but the low-resolution prior information from GOCO05s (cf. section 2.5) mainly serves for stabilizing the inversion and downward continuation process, in order to reduce rank deficiency and singularity problems (cf. section 3.1.4).

4.3. Resulting Coefficients

The unknown coefficients d_q are finally estimated by inserting the iterated VCs $\hat{\sigma}_k^2$ and $\hat{\sigma}_d^2$ into equation (16). From the resulting coefficient vector $\hat{\mathbf{d}}_L$, we compute different functionals of the Earth's gravity field in our target area. Figure 5a shows the 2118 coefficients covering the computation area $\partial\Omega_C$. Inside $\partial\Omega_I$ (green bordered) the 1000 coefficients themselves already represent the gravitational structures. Consequently, they have a physical meaning: large (positive or negative) values indicate additional gravity signal with respect to the background model. Inside $\partial\Omega_I$, the coefficients vary between $-1.31 \text{ m}^2/\text{s}^2$ and $2.15 \text{ m}^2/\text{s}^2$; their standard deviations $\sqrt{\hat{v}(\hat{d}_q)}$ (Figure 5b), obtained from the main diagonal elements of \mathbf{Q}_{dd}^{-1} (17), between $0.39 \text{ m}^2/\text{s}^2$ and $0.65 \text{ m}^2/\text{s}^2$. (The numbers are given in SI unit m^2/s^2 after scaling the design matrices \mathbf{A}_k and reducing the observations by a mean value.) The standard deviations are about 1 order of magnitude smaller than the coefficients, indicating a good S/N ratio and thus a well-balanced combination of the data sets.

As expected, the coefficients outside from the target area $\partial\Omega_I$ alternate and get an artificial character. Values from $-2.15 \text{ m}^2/\text{s}^2$ to $4.34 \text{ m}^2/\text{s}^2$ are reached in the margin between $\partial\Omega_I$ and $\partial\Omega_C$, and the standard deviations increase up to $0.97 \text{ m}^2/\text{s}^2$. We discuss this effect in section 4.5.1.

4.4. Final Gravity Functionals and Their Statistics

Gravity functionals $\mathcal{Y}[V] = z(\mathbf{x}^c)$ are obtained by solving the general synthesis equation (18) at any point of interest with location $\mathbf{x}^c \in \partial\Omega_I$. In the synthesis step we multiply the estimated coefficient vector $\hat{\mathbf{d}}_L$ from equation (16) with low-pass filtering Blackman scaling functions to remove high-resolution artifacts. We compute exemplarily both gravity anomalies Dg (see Figure 6) and quasi-geoid heights ζ (see Figure 7) in the target area $\partial\Omega_I$ on a regular grid with spatial resolution of 0.05° . The corresponding statistics and standard deviations, derived by error propagation according to equation (20), give a measure for the precision of the

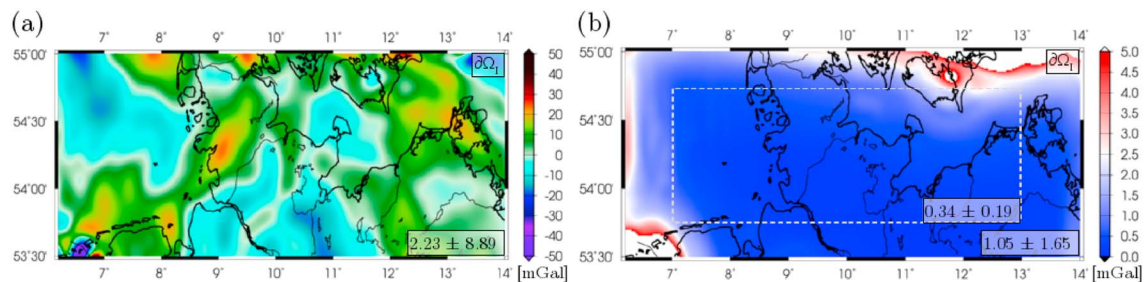


Figure 6. (a) Differential gravity anomalies Dg up to level $J = 11$, referenced to GOCO05s up to $j = 7$, and the (b) corresponding standard deviations. Mean values and their standard deviations (depicted in boxes, given in mGal) are computed for $\partial\Omega_I$ in Figures 6a and 6b, and for an inner region in Figure 6b (dashed box) representing the above all well-observed study area.

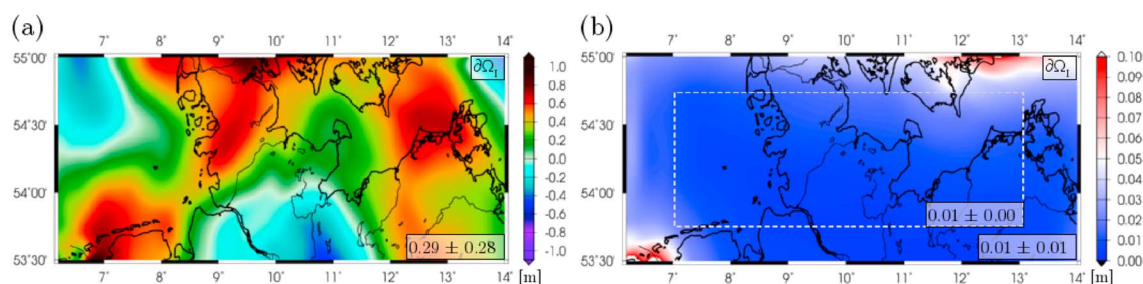


Figure 7. (a) Differential quasi-geoid heights ζ up to level $J = 11$, with respect to GOCO05s up to $j = 7$, and their (b) standard deviations. The statistics (depicted in boxes) are given accordingly to Figure 6.

modeling result. An external evaluation is given in the next section 4.5 by a validation against global models, against a regional model, and a cross validation against excluded data.

4.4.1. Gravity Anomalies

The resulting gravity anomalies Dg , shown in Figure 6a, vary in a range of around ± 30 mGal with respect to GOCO05s (d/o 127), except in the southwest corner, where edge effects with values down to -57.22 mGal prevail due to data gaps. In principle, the largest negative anomalies of the differential signal are located in the south of the target area at around 11° longitude and in the northwestern edge of $\partial\Omega_i$. Some spatially more limited positive anomalies appear along the coastlines at the mouths of rivers in the North Sea, in the Baltic Sea between 12° and 13° longitude, and at the northern boundary of the target area (at $8^\circ, 9.5^\circ$, between 12° and 13° longitude). The respective standard deviations in Figure 6b show here, however, their largest values with amplitudes of >5 mGal, indicating a low precision of the modeling result. This might be an artifact resulting from data gaps in the airborne measurements. Figure 1 shows clearly missing tracks in these regions. Large standard deviations further appear in the southwest corner because of missing observations in the *Netherlands*. Data sets should overlap the target area in general (cf. section 3.1.3) to avoid such erroneous edge effects. However, within the mainly well-observed area (dashed line in Figure 6b), the standard deviations are very small: we obtain on average 0.34 mGal (maximum 1.76 mGal). As we introduced in section 4.1 all weighting matrices as unit matrices in the estimation model (14), we have to take into account that the error propagation (cf. equation (19)) might deliver too positive error estimates by neglecting possibly correlations between the measurements. A more realistic stochastic model could further marginally change the relative weighting between the observation groups. However, we conclude that we derive a modeling result with high internal precision.

We remove the erroneous edge effects in the southwest and northeast corners according to the standard deviations and obtain gravity anomalies from -21.17 mGal to 25.45 mGal, i.e., on average 2.21 ± 8.45 mGal. Restoring GOCO05s delivers the total spectral content ($l = 0, \dots, 2047$) of the gravity signal in the study area, see Figure 8a. The range of Dg counts -32.85 mGal to 34.00 mGal with a mean value of -4.44 ± 12.63 mGal. Comparing the total with the differential signal shows, as expected, rising amplitudes of Dg due to the restored long wavelengths of GOCO05s. The structures change especially in the North Sea: positive anomalies along the southern coastline in Figure 6a are overlaid by a strong negative anomaly in Figure 8a. As we assume the background model to be noise free, the standard deviations from Figure 6b do not change. We validate this total gravity signal by comparisons with existing global models in section 4.5.1.

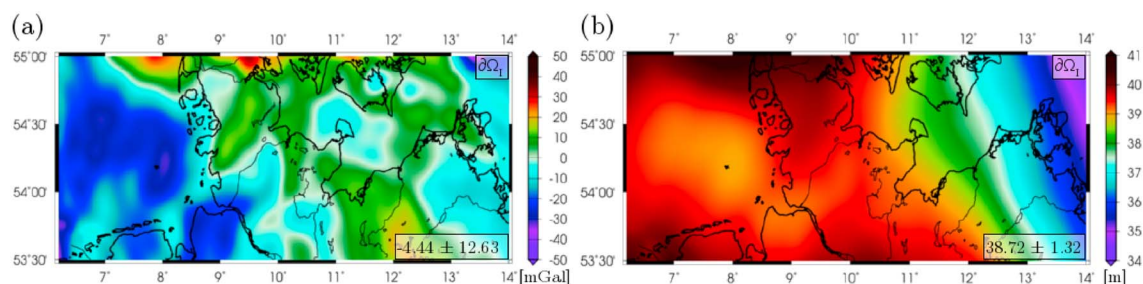


Figure 8. (a) Total gravity anomalies Dg and (b) quasi-geoid heights ζ up to level $J = 11$ (background model GOCO05s restored). The mean values and the standard deviations of the mean values (depicted in boxes) are given in the corresponding units.

Table 3. Differences Between Regional Results (reg) at Level $J = 11$, Blackman Filtered up to $l = 2047$, Outliers Removed, and the Corresponding Functionals Dg and ζ Computed From EGM2008 (EGM) and EIGEN-6c (EIG), Both Blackman Filtered up to Level $J = 11$ ^a

Difference	Range	Mean	SD	Relative SD
ΔDg (reg-EGM)	−21.96 to 14.46 mGal	−0.68 mGal	2.30 mGal	18.1%
ΔDg (reg-EIG)	−20.97 to 15.46 mGal	−0.61 mGal	2.41 mGal	19.0%
$\Delta \zeta$ (reg-EGM)	−0.08 to 0.40 m	0.09 m	0.06 m	4.3%
$\Delta \zeta$ (reg-EIG)	−0.04 to 0.43 m	0.10 m	0.05 m	4.1%

^aThe relative standard deviation (SD) is referenced to the standard deviation of the mean value of EGM2008 in $\partial\Omega_r$.

4.4.2. Quasi-Geoid Heights

The differential quasi-geoid heights ζ (with respect to GOCO05s, d/o 127) in Figure 7a show similar structures as the differential gravity anomalies (Figure 6a), since they are related to the same set of coefficients $\hat{\mathbf{d}}_L$. However, the field transformation smooths the gravity signal: the functional ζ is normalized by a normal gravity γ (here with respect to GRS80) and thus represents less spatial details. Minimum values are reached in the German lowlands down to −0.48 m with respect to GOCO05s. Maximum values up to 1.06 m appear mainly at the same locations as the maximum values of gravity anomalies. The corresponding standard deviations (Figure 7b) increase up to maximum 0.12 m along the northern borderline and in the southwest corner due to the data gaps, as discussed in section 4.4.1. Within the well-observed inner area (dashed box), the mean value of the standard deviations of only 1 cm (maximum 2.2 cm) approves the high internal precision of the modeling approach, taking into account feasibly too positive error estimates. According to the outlier detection in section 4.4.1, we obtain finally a signal from −0.48 m to 0.90 m with a mean value of 0.28 ± 0.28 m with respect to GOCO05s.

While gravity anomalies with their detailed gravitational structures are often used for a spectral analysis, (quasi-) geoid heights serve mainly as reference for height systems. Thus, restoring the previously subtracted background model GOCO05s is more important here to obtain the total gravity signal $l = 0, \dots, 2047$, see Figure 8b. The amplitudes vary between 34.40 m and 40.73 m and indicate the total height above the reference ellipsoid GRS80.

4.5. Validation

The external accuracy of the computed functionals can be assessed, e.g., by comparing the regional results (1) with high-resolution global SH models, (2) with an existing regional model computed by a different approach and/or from different input data, or (3) by composing a cross validation, i.e., extracting some input data from the estimation and comparing the modeling results finally with those data. A comparison with regional models should proof the plausibility of our solution, while differences to existing global models identify supplementary significant signal content in our model and thus the additional value of the chosen approach. However, we have to take into account correlations between identical input data in the different models. The cross validation further allows rating the model fit of the data and thus the external accuracy. We present and discuss the results of the three strategies in the following.

4.5.1. Comparison With Global Models

We choose two global high-resolution models, EGM2008 (EGM), available up to d/o 2190, and EIGEN-6c (EIG), available up to d/o 1949, and computed the differences ΔDg and $\Delta \zeta$ to our total regional (reg) results (outliers removed, background model GOCO05s restored) of Dg and ζ . For spectral consistency, we smoothed the equivalent functionals of the global SH models with the same Blackman filter up to degree $l_{11} = 2047$, as we used in the regional synthesis (cf. section 3.2.2). (The missing high frequencies $l = 1950, \dots, 2047$ in the EIGEN-6c model are set to zero and do not influence the applied Blackman filter.) Table 3 lists the range, the mean values, and the corresponding (relative) standard deviations of the differences (reg-EGM) and (reg-EIG) for the target area $\partial\Omega_r$. In general, the differences to EGM2008 and to EIGEN-6c are comparable. (The difference between both global models counts ΔDg (EGM-EIG) = 0.07 ± 0.94 mGal, $\Delta \zeta$ (EGM-EIG) = 0.5 ± 3.0 cm, respectively, resulting mainly from the different spectral resolution.) The mean values of the differences of −0.68 mGal for ΔDg (reg-EGM) (−0.61 mGal for ΔDg (reg-EIG)) and 0.09 m for $\Delta \zeta$ (reg-EGM) (0.10 m for $\Delta \zeta$ (reg-EIG)) indicate a small offset, probably stemming from the spatially limited data sets used in the regional solution and from insufficient prior information, and thus missing information in the middle frequencies.

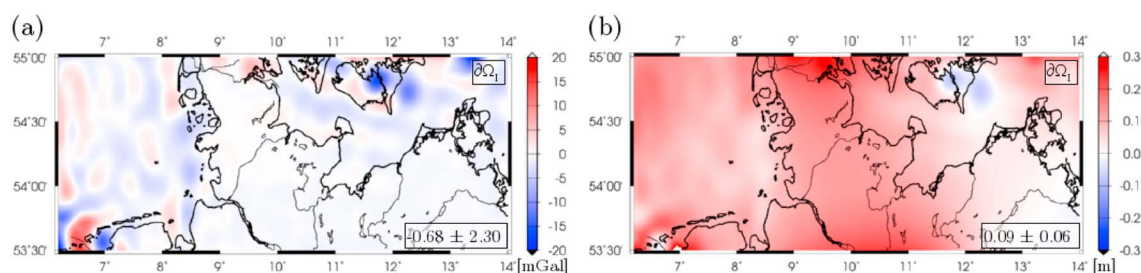


Figure 9. Differences (a) ΔDg and (b) $\Delta \zeta$ of the resulting total gravity anomalies and quasi-geoid heights (cf. Figure 8, background model GOCO05s restored) to the global model EGM2008, consistently filtered with Blackman kernel up to degree $l_{11} = 2047$. Mean values and standard deviations from the mean values are given for $\partial \Omega_1$ in the corresponding units.

The according standard deviations of 2.30 mGal and 2.41 mGal (corresponding to EGM2008 and EIGEN-6c) from the mean value of the gravity anomaly differences are 1 order of magnitude larger than the mean values themselves. For quasi-geoid heights they are with 6 cm (EGM) and 5 cm (EIG) similar to the mean values. In order to compare the different output functionals, we computed relative standard deviations related to the standard deviation (12.67 mGal for Dg and 1.32 m for ζ) of the mean value of the EGM2008 signal as well. Thus, the relative standard deviation counts around 18.1% for gravity anomaly differences ΔDg (reg-EGM), but just around 4.3 % for quasi-geoid height differences $\Delta \zeta$ (reg-EGM). We explain the lower relative standard deviation of $\Delta \zeta$ by the smoothness of the functional ζ itself (cf. section 4.4.2), whereas the differential gravity quantity Dg shows much more detailed structures. The dependency of the differences (reg-EGM) and (reg-EIG) on field transformations could indicate a higher signal content in our regional model: Potential erroneous modeling effects would influence the different functionals Dg and ζ to equal parts, which is obviously not the case in the chosen study area.

To further proof this, we study the spatial pattern of the differences ΔDg and $\Delta \zeta$ to EGM2008 (reg-EGM), see Figures 9a and 9b. As expected, the largest deviations (down to -22 mGal for gravity anomalies and up to around 40 cm for quasi-geoid heights) occur in the southwest corner where our regional model contains erroneous edge effects due to the lack of data. Comparing the spatial pattern with the observations in Figure 1, we notice that the terrestrial data end up along the borderline of the Netherlands, and the airborne tracks do not overlap $\partial \Omega_1$ along the northern margin. Those dominant local effects coincide with the largest standard deviations in Figures 6b and 7b. Thus, we conclude a lack of signal content in our regional model. The low-resolution prior information obtained from GOCO05s up to d/o 127 cannot provide enough spectral information to overcome these edge effects. For $\Delta \zeta$ the offset of around 10 cm predominates the remaining small standard deviations (Figure 9b), while for the more sensitive differences ΔDg some small-scale structures occur especially in the offshore areas. We interpret those deviations as additional signal in our regional model, stemming especially from altimetry observations (mainly Cryosat and Jason-1 GM), and from airborne measurements, which overcome the altimetry data gaps near the coastlines. They are not part of the global model EGM2008. Over land, our regional model and the global EGM2008 model fit better. For the remaining deviations, correlations stemming from terrestrial and airborne data sets can be excluded, as we used recently collected data which are not contained in the existing global models (EGM2008 relies on older data with less accuracy). Hence, we interpret the differences as supporting information in our regional model as well. We conclude from the small standard deviations in Figures 6b and 7b a high precision of our model and its potential to improve the existing global models in selected regions.

4.6. Comparison With a Regional Model

While global models fit global data sets very well, regional gravity models aim to fit high-resolution spatially limited data sets with high precision. In order to validate our regional modeling result, we thus compare it to an existing regional model, the *German Combined Quasigeoid 2011* (GCG2011). It is provided by BKG and IfE (Institut für Erdmessung der Leibniz Universität Hannover) and represents the official German height reference with an offshore precision of 4 cm to 10 cm and an onshore precision of 1 cm to 2 cm in the German lowlands (source: Documentation from 28 December 2011, BKG Leipzig, Abteilung Geodäsie, <http://www.geodatenzentrum.de/docpdf/quasigeoid.pdf>, in German). Thus, the precision is comparable with the obtained mean standard deviation of 1 cm of our regional model, cf. Figure 7b.

Table 4. Differences of the Quasi-Geoid Heights Obtained by Our Regional Approach (reg) up to Level $J = 11$, Blackman Filtered up to $l_{11} = 2047$, to GCG2011 (GCG), as Well as to EGM2008 (EGM), Also Blackman Filtered up to $l_{11} = 2047$ ^a

Difference	Range	Mean	SD	Relative SD
$\Delta\zeta$ (reg-GCG)	−0.38 to 0.20 m	−0.18 m	0.06 m	4.8%
$\Delta\zeta$ (EGM-GCG)	−0.38 to −0.15 m	−0.28 m	0.03 m	2.3%

^aThe values $\Delta\zeta$ are computed at the given $1' \times 1.5'$ GCG2011 grid. The relative standard deviation is referenced to the standard deviation of the mean value of EGM2008.

The statistics of all differences are listed in Table 4. The mean value of the difference $\Delta\zeta$ (reg-GCG) between our regional estimation (reg) and the GCG2011 model (GCG) predominates with -18 cm the small standard deviations of $\leq 5\%$, relatively to the mean standard deviation of EGM2008. Comparing the global EGM2008 model (EGM) with GCG2011 delivers a larger offset of -28 ± 3 cm, but an even smaller relative standard deviation of 2.3%. The difference seems to originate from the GCG2011 model, as the difference $\Delta\zeta$ (reg-EGM) at exactly the same grid points counts a mean value of 9 ± 6 cm, equivalent to the corresponding statistics in Table 3. In contrast to our regional model, the GCG2011 is not a pure gravimetric geoid model, as it is adapted to a number of GNSS (Global Navigation Satellite System) leveling points in order to allow transformations to geometric reference frames.

We further evaluate the differences for different subregions, shown in Figure 10. The offset increases between the western (green bordered box from 6.2° to 10° longitude) and the eastern part (10° to 14° longitude) from -14 cm to -22 cm. The mean standard deviations of the differences increase as well, but they differ additionally between offshore and onshore regions: Over the North Sea, mainly observed by altimetry (gray dashed box from 6.2° to 8° longitude), they count 2 cm from the mean value and 4 cm for the entire green bordered western part, containing both offshore and onshore areas. Over the Baltic Sea they rise up to 5 cm, and we obtain finally 7 cm over the southeast “terrestrial-only” area (gray dashed box). Comparing those values with the given precision of the GCG2011 model, the differences $\delta\zeta$ (reg-GCG) are not significant in offshore areas, but over land. As the GCG2011 relates to the same terrestrial, airborne, and shipborne input data sets as our regional model, the deviations may result from topographic corrections which have been applied to the GCG2011 model (source: <http://www.geodatenzentrum.de/docpdf/quasigeoid.pdf>).

However, regarding the whole area $\partial\Omega$, both regional models fit very well to each other, and the small standard deviation (6 cm) of the mean difference confirms the high precision of our modeling result.

4.6.1. Cross Validation

In order to evaluate the external accuracy of our regional model, we set up a cross validation: we excluded the altimetry Envisat EM observations and recomputed quasi-geoid heights at their 1029 positions. We choose Envisat EM among all altimetry missions, as it does not affect the spatial extent of the satellite data, especially the coverage of the Baltic Sea and the areas along the coastlines. The differences $\Delta\zeta^\#$ to the eliminated altimeter observations are displayed in Figure 11a. Further, we excluded each tenth shipborne and each tenth terrestrial observation and recomputed gravity anomalies at their locations. Figures 11b and 11c show the

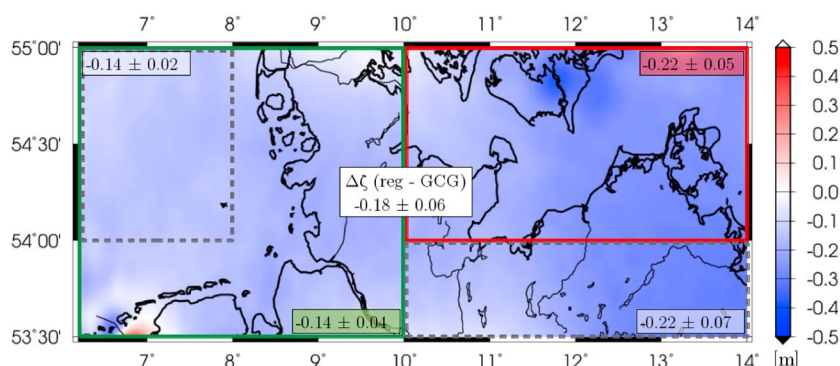


Figure 10. Differences $\Delta\zeta$ of the resulting quasi-geoid heights up to level $J = 11$ (GOCO05s restored), cf. Figure 8b, and the regional GCG2011 model. Mean values and their standard deviations are computed for different areas: the entire area, the altimetry validation area (red box), the shipborne validation area (green box), and one pure offshore, as well as one pure onshore area (gray dashed boxes).

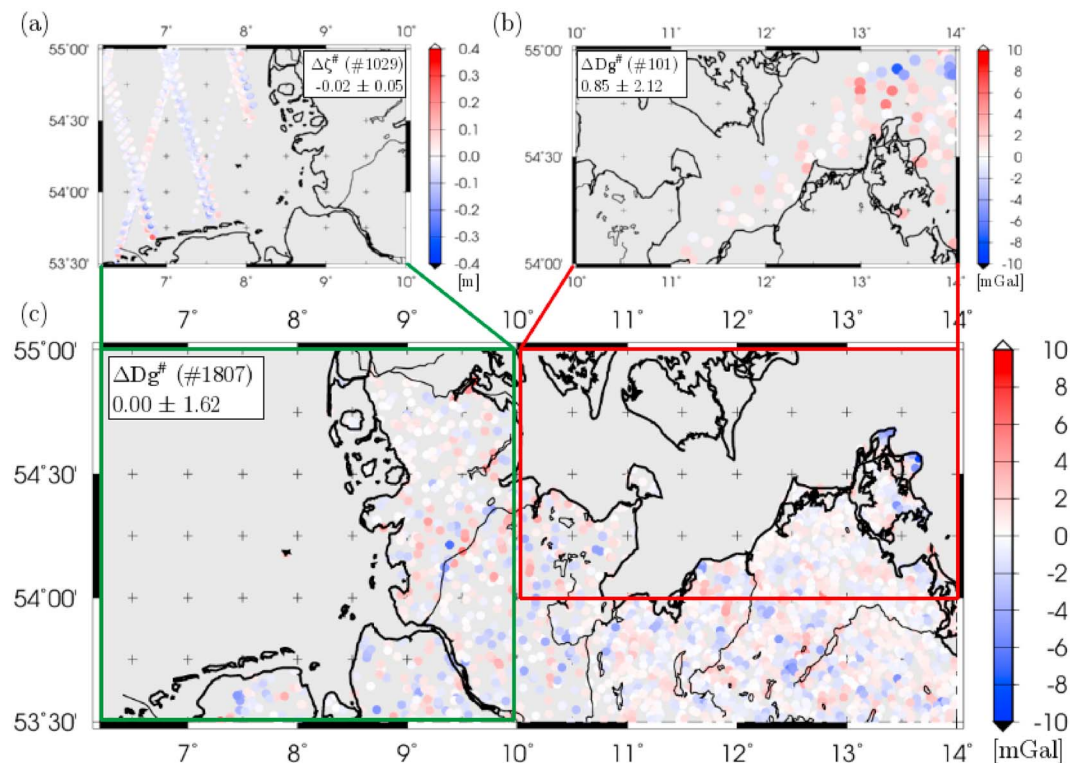


Figure 11. Cross validation with (a) 1029 Envisat EM (Env), (b) 101 shipborne (ship), and (c) 1807 terrestrial (terr) observations. Displayed are the differences $\Delta\zeta^{\#}$ (reg-Env) (Figure 11a), $\Delta Dg^{\#}$ (reg-ship) (Figure 11b), and $\Delta Dg^{\#}$ (reg-terr) (Figure 11c) between the observations and the modeled total gravity functionals (reg), computed without these observations, at locations of the validation data sets. Mean values and their standard deviations are given in the corresponding units m (Figure 11a) and mGal (Figures 11b and 11c).

corresponding differences $\Delta Dg^{\#}$ (reg-ship) and $\Delta Dg^{\#}$ (reg-terr) at the 101 and 1807 data points. Table 5 lists the statistics of the cross validation.

Envisat EM data. For the cross validation with Envisat EM (reg-Env) we notice a very homogeneous structure of the differences (cf. Figure 11a) with a mean value of -2 ± 5 cm, excluding a few outliers >30 cm, close to the islands in the south. In this coastal area, we assume the altimeter data to be erroneous (cf. section 2.4). The standard deviations of the mean values of both differences (reg-Env) and (EGM-Env) count 5 cm, i.e., 4.1% of the mean standard deviation of the EGM2008 signal, see Table 5. The small relative deviation states a high external precision of our regional model with respect to Envisat EM observations. To consistently compare the

Table 5. Statistics of the Cross Validation: Differences $\Delta\zeta$ and ΔDg Between the Total Regional Model (reg) and the Previously Excluded (a) 1037 Envisat EM (Env), (b) 101 Shipborne (ship), and (c) 1807 Terrestrial (terr) Data (cf. Figure 11)^a

Difference	Range	Mean	SD	Relative SD
$\Delta\zeta^{\#}$ (reg-Env)	-0.28 to 0.25 m	-0.02 m	0.05 m	4.1%
$\Delta\zeta^{\#}$ (EGM-Env)	-0.36 to 0.15 m	-0.12 m	0.05 m	4.1%
$\Delta\zeta^{\#}$ (reg-EGM)	0.05 to 0.17 m	0.10 m	0.03 m	2.3%
$\Delta Dg^{\#}$ (reg-ship)	-7.55 to 5.50 mGal	0.85 mGal	2.12 mGal	16.7%
$\Delta Dg^{\#}$ (EGM-ship)	-2.32 to 5.69 mGal	2.46 mGal	1.62 mGal	12.8%
$\Delta Dg^{\#}$ (reg-EGM)	-10.11 to 3.44 mGal	-1.61 mGal	1.77 mGal	14.0%
$\Delta Dg^{\#}$ (reg-terr)	-9.02 to 6.97 mGal	0.00 mGal	1.62 mGal	12.8%
$\Delta Dg^{\#}$ (EGM-terr)	-7.79 to 5.60 mGal	0.52 mGal	1.59 mGal	12.5%
$\Delta Dg^{\#}$ (reg-EGM)	-3.36 to 5.18 mGal	-0.52 mGal	0.48 mGal	3.8%

^aAdditionally, we compare the global model EGM2008 (EGM) with both the data sets and the regional results. Relative standard deviations are referenced to the standard deviation of the mean value of EGM2008 in $\partial\Omega_i$.

cross validation with the validation against EGM2008 (cf. section 4.5.1), we recomputed the differences along the Envisat EM tracks and obtain a relative standard deviation (reg-EGM) of 2.3%. We conclude that over the ocean our regional model fits better to the global model EGM2008 than to the Envisat EM observations, but both models, the global EGM2008 and our regional model, fit the altimetry observations similarly. We do not achieve an improvement with our regional approach in the case of fitting altimeter data sets, but we reach comparable precision as with a global approach and even higher accuracy comparing the mean values of the differences of -2 cm for (reg-Env) versus -12 cm for (EGM-Env).

Terrestrial data. In the case of fitting regional data sets, we reach similar relative approximations: In a second cross validation we compare our regional model with the excluded 1807 (10 %) terrestrial observation sites. From Table 5 we infer that our regional model (reg) fits the terrestrial data (terr) again equivalently to the global EGM2008 model (EGM) (relative standard deviations of 12.8% and 12.5%). However, mean value of the differences $\Delta Dg^{\#}$ (reg-terr) counts 0.00 ± 1.62 mGal, whereas $\Delta Dg^{\#}$ (EGM-terr) delivers 0.52 ± 1.59 mGal. As the differences $\Delta Dg^{\#}$ (reg-terr), displayed in Figure 11c, do not show any systematic, we conclude that our model confidently extracts as much information as possible from the regional data set.

Shipborne data. From the cross validations with Envisat EM and with terrestrial data we conclude a similar modeling precision both by a global and by a regional approach. To further proof, if the model approximations are independently from onshore or offshore areas, we set up a cross validation with 101 shipborne data, see Figure 11b. The corresponding statistics of the differences $\Delta Dg^{\#}$ (reg-ship) in Table 5 show a larger relative standard deviation (16.7%) than the differences (reg-terr) to terrestrial data. It seems reasonable, as the shipborne data have minor accuracy than the terrestrial and thus get a smaller weight in the VCE, cf. Table 2. The data fit by our regional model is less close than the data fit by the EGM2008 model (12.8% relative standard deviation of the differences). Assuming the large differences in the northeast corner stemming from erroneous edge effects (cf. large standard deviations in Figure 6b) and excluding them delivers a standard deviation of 1.24 mGal (9.8%). We conclude that our regional approach approximates high-resolution spatially limited data sets for both onshore and offshore areas very well, by (1) exploiting the signal content and (2) combining them as optimally as possible.

5. Summary and Outlook

We set up a regional gravity modeling approach using radial spherical basis functions from the combination of heterogeneous data sets. For our studies in Northern Germany we developed an estimation model based on Shannon and Blackman functions in terms of series expansion up to degree $L = 2190$ ($l_{11} = 2047$ in the synthesis). From the results, the error propagation and the validation, we summarize the following aspects:

1. We are able to model any functional of the gravitational potential (in any height above the Earth's surface) by formulating appropriate observation equations. As expected, gravity anomalies show more structure than (quasi-)geoid heights (cf. section 4.4). The corresponding, reliable standard deviations are about 1 order of magnitude smaller than the functionals, indicating significant results. The largest standard deviations occur close to data gaps, at the borderline of the target area, which seems reasonable.
2. The VCE in section 4.2 delivers a realistic relative weighting of the different data sets. We conclude that it is an appropriate tool to reach our aim of a well-balanced spectral combination of data sets with different accuracies, resolutions, and distributions. However, the spectral content and the missing stochastic information of the introduced prior information (for regularization purposes) stemming from GOCO05s is not sufficient to fill in data gaps at $J = 11$. For the future, we plan to extract prior information from other data sources, as, e.g., topographic models.
3. The results in section 4.4 verify the tools and settings of our approach, presented in section 3.1, by showing a good internal accuracy and precision derived from error propagation. Mean standard deviations of 0.34 mGal for Dg and 0.01 m for ζ , are reached in the inner, well-observed part of the study area.
4. The cross validation with altimetry observations from Envisat EM, with terrestrial data and with shipborne data, delivers maximum standard deviations of 5 cm and 2.12 mGal, attesting the high precision and quality of our regional model. The differences to the global EGM2008 model at the same validation sites deliver comparable deviations. We conclude that our regional approach is able to extract the signal content of heterogeneous observation techniques as optimally as possible.
5. The differences between our regional solution and the SH model EGM2008 (cf. section 4.5.1) yield relative standard deviations of around 18.1% difference for ΔDg and around 4.3% difference for $\Delta \zeta$. From the larger

relative standard deviations of the more sensitive functional Dg (compared with the smoother functional ζ), we suppose that the differences might indicate additional signal in the regional model.

6. The plausibility of our solution is proofed by the comparison with the regional quasi-geoid GCG2011 model: We obtain small deviations of a few centimeters. We notice slightly larger deviations over land, probably stemming from a topographic reduction applied to GCG2011. Further studies in mountainous regions, together with the use of a topographic model as prior information, are planned.

The remaining differences of the comparisons of our regional solution with the validation data and with the global solutions might result from (1) the lack of knowledge of correlations of the observations and thus an incomplete stochastic model, (2) artificial effects stemming from the oscillations and truncation of the basis functions, (3) remaining rank deficiency problems that may cause numerical instabilities, and (4) the lack of knowledge of the exact spectral resolutions of the input data sets and their varieties, which leads to a compromise in the choice of the modeling resolution.

As the effects are very small, we conclude that we reached the aim of setting up a regional gravity modeling approach, being both spatially and spectrally as close as possible to the observations and extracting a high degree of information from an appropriate combination of the different data sets. In contrast to the rigorous combination at one level J presented here, a spectral combination at different levels might optimize the results. We plan further investigations by applying a MRR (mentioned in section 3.1.5) and implementing a pyramid algorithm for a step-by-step combination of those observations [see Schmidt et al., 2015], which contribute most at corresponding resolution levels.

Acknowledgments

The authors like to thank the Bundesamt für Kartographie und Geodäsie (BKG) and the federal states Schleswig-Holstein, Mecklenburg West-Pomerania, and Lower Saxony for providing us the terrestrial, airborne, and shipborne data sets. Further, we appreciate the availability of the German Combined Quasi-geoid 2011 (GCG) through the BKG, especially Gunter Liebsch and Uwe Schirmer. The data are available by contacting the corresponding persons at BKG (gunter.liebsch@bkg.bund.de, heinz-uwe.schirmer@bkg.bund.de). The altimetry data were generated by DGF-TUM and are freely available through <http://openadb.dgf.tum.de/index.php?id=123>. The satellite gravimetry models can be publicly accessed from <http://icgem.gfz-potsdam.de/ICGEM/>. We also thank the anonymous reviewers and the Editor Paul Tregoning for their valuable input.

References

- Bentel, K., M. Schmidt, and C. Gerlach (2013a), Different radial basis functions and their applicability for regional gravity field representation on the sphere, *Int. J. Geomath.*, **4**, 67–96, doi:10.1007/s13137-012-0046-1.
- Bentel, K., M. Schmidt, and C. Rolstad Denby (2013b), Artifacts in regional gravity representations with spherical radial basis functions, *J. Geod. Sci.*, **3**(3), 173–187, doi:10.2478/jogs-2013-0029.
- Bosch, W., R. Savcenko, D. Dettmering, and C. Schwatke (2013), A two decade time series of eddy-resolving dynamic ocean topography (iDOT), in *Proceedings of the ESA symposium on 20 Years of Progress in Radar Altimetry, Venice, Italy, ESA Spec. Publ. SP710*, edited by L. Ouwehand, ESA/ESTEC, Noordwijk, Netherlands.
- Bosch, W., D. Dettmering, and C. Schwatke (2014), Multi-mission cross-calibration of satellite altimeters: Constructing a long-term data record for global and regional sea level change studies, *Remote Sens.*, **6**(3), 2255–2281, doi:10.3390/rs6032255.
- Boucher, C., and Z. Altamimi (1992), Terrestrial Reference System and its first realizations, *Astronomisch-Geodätische Arbeiten*, **52**, 205–213, Bayerische Kommission für die internationale Erdmessung.
- Eicker, A., J. Schall, and J. Kusche (2013), Regional gravity modelling from spaceborne data: Case studies with GOCE, *Geophys. J. Int.*, **196**(3), 1431–1440, doi:10.1093/gji/ggt485.
- Freeden, W. (1999), *Multiscale Modelling of Spaceborne Geodata*, Teubner Stuttgart, Leipzig, Germany.
- Freeden, W., and V. Michel (2001), Basic aspects of geopotential field approximation from satellite-to-satellite tracking data, *Math. Method Appl. Sci.*, **24**(11), 827–846, doi:10.1002/mma.244.
- Freeden, W., T. Gervens, and M. Schreiner (1998), *Constructive Approximation on the Sphere (With Applications to Geomathematics)*, Oxford Sci. Publ., Clarendon Press, Oxford.
- Haagmans, R., K. Prijatna, and O. D. Omang (2002), An alternative concept for validation of GOCE gradiometry results based on regional gravity, paper presented at 3rd Meeting of International Gravity and Geoid Commission, Thessaloniki Greece.
- Koch, K.-R. (1977), Least squares adjustment and collocation, *Bull. Geod.*, **51**(2), 127–135, doi:10.1007/BF02522282.
- Koch, K.-R., and J. Kusche (2002), Regularization of geopotential determination from satellite data by variance components, *J. Geod.*, **76**, 259–268, doi:10.1007/s00190-002-0245-x.
- Krupar, T. (1970), The method of least squares collocation, *Stud. Geophys. Geod.*, **14**(2), 107–109, doi:10.1007/BF02585604.
- Mayer-Gürr, T., et al. (2015), The combined satellite gravity field model GOCO05s, Abstracts 12364 presented at 2015 EGU General Assembly, Vienna, Austria, 12–17 Apr.
- Morelli, C., C. Gantar, R. K. McConnell, B. Szabo, and U. Uotilaet (1971), *The International Gravity Standardization Net 1971 (I.G.S.N.71)*, IUGG IAG Spec. Publ. SP-4, Int. Assoc. of Geod., Paris, France.
- Moritz, H. (1978), Least-squares collocation, *Rev. Geophys. Space Phys.*, **16**(3), 421–430.
- Moritz, H. (2000), The Geodesist's handbook 2000, *J. Geod.*, **74**, 1.
- Naeimi, M. (2013), Inversion of satellite gravity data using spherical radial base functions, PhD thesis, Germany.
- Neunhöfer, H., M. Börngen, A. Junge, and J. Schweitzer (1997), Zur Geschichte der Geophysik in Deutschland, Jubiläumsschrift zur 75jährigen Wiederkehr der Gründung der Deutschen Geophysikalischen Gesellschaft, Deutsche Geophysikalische Gesellschaft, Hamburg.
- Pail, R., et al. (2010), Combined satellite gravity field model GOCO01S derived from GOCE and GRACE, *Geophys. Res. Lett.*, **37**, L20314, doi:10.1029/2010GL044906.
- Panet, I., A. Chambodut, M. Diamant, M. Holschneider, and O. Jamet (2006), New insights on intraplate volcanism in French Polynesia from wavelet analysis of GRACE, CHAMP and sea-surface data, *J. Geophys. Res.*, **111**, B09403, doi:10.1029/2005JB004141.
- Pavlis, N. K., S. A. Holmes, S. C. Kenyon, and J. K. Factor (2012), The development and evaluation of the Earth Gravitational Model 2008 (EGM2008), *J. Geophys. Res.*, **117**, B04406, doi:10.1029/2011JB008916.
- Reguzzoni, M., and F. Sansò (2012), On the combination of high-resolution and satellite-only global gravity models, *J. Geod.*, **86**, 393–408, doi:10.1007/s00190-011-0526-3.
- Reuter, R. (1982), Über Integralformeln der Einheitssphäre und harmonische Splinesfunktionen, PhD thesis, RWTH Aachen, Germany.

- Rummel, R., G. Balmino, J. Johannessen, P. Visser, and P. Woodworth (2002), Dedicated gravity field missions—Principle and aims, *J. Geodyn.*, 33(1–2), 3–20, doi:10.1016/S0264-3707(01)00050-3.
- Schmidt, M., M. Fengler, T. Mayer-Gürr, A. Eicker, J. Kusche, L. Sánchez, and S. C. Han (2007), Regional gravity modeling in terms of spherical base functions, *J. Geod.*, 81(1), 17–38, doi:10.1007/s00190-006-0101-5.
- Schmidt, M., F. Göttl, and R. Heinkelmann (2015), Towards the combination of data sets from various observation techniques, *Int. Assoc. Geod. Symp.*, 140, 35–43, doi:10.1007/978-3-319-10828-5_6, Springer Intl. Publishing Switzerland.
- Schreiner, M. (1996), A pyramid scheme for spherical wavelets, *AGTM-Rep. 170*, Laboratory of Technomathematics, Geomathematics Group, Department of Mathematics, Univ. of Kaiserslautern, Germany.
- Tapley, B. D., S. Bettadpur, M. Watkins, and C. Reigber (2004), The gravity recovery and climate experiment: Mission overview and early results, *Geophys. Res. Lett.*, 31, L09607, doi:10.1029/2004GL019920.
- Weber, D. (1994), Das neue gesamtdeutsche Haupthöhennetz DHHN 92, *Allg. Vermessungs-Nachrichten: AVN*, 101(5), 179–193, Zeitschrift für alle Bereiche der Geodäsie und Geoinformation, Berlin Wichmann, VDE Verlag.